
Article:
Copley, R.J. and Dwyer-Joyce, R.S. orcid.org/0000-0001-8481-2708 (2023) Prediction of the internal structure of a lithium-ion battery using a single ultrasound wave response. Journal of Energy Storage, 72, Part E. 108778. ISSN 2352-152X

https://doi.org/10.1016/j.est.2023.108778

Prediction of the internal structure of a lithium-ion battery using a single ultrasound wave response

R.J. Copley and R.S. Dwyer-Joyce.

Department of Mechanical Engineering, University of Sheffield, Sheffield, UK.

Abstract

This paper describes a means to predict the internal structure of a lithium-ion battery from its response to an acoustic impulse, using a machine learning algorithm. Lithium-ion batteries are sealed components and the internal states of the cell such as charge, health, and presence of structural defects are difficult to measure. Ultrasonic inspection of lithium-ion batteries is a recent and growing area of research. Reflected and transmitted ultrasound pulses are proposed as a non-invasive means of gaining insights into the internal structure and changes within the closed body of a cell. However, the multiple layers present in a lithium-ion cell are problematic when attempting to interpret waveforms as many internal reflections superimpose. Attributing specific features of a cell to wave characteristics is challenging.

In this work a genetic algorithm has been developed as a means to reverse engineer a single ultrasound wave response to predict the internal layered structure of a lithium-ion battery cell. A first randomised guess at the layered structure is made. A numerical wave propagation model is used to predict the ultrasound waveform associated with that structure. This waveform is then compared with a measured or reference waveform to establish its fitness. The layered structure is generationally mutated until the predicted waveforms converge on the reference signal. As this occurs the predicted layered body reveals insights into the cell structure under inspection.

Initially, the algorithm was tested against an idealised model battery and its predicted waveform, giving a model-model verification. Further, experimental ultrasonic reflection signals were captured from small capacity lithium-ion cells. Estimations of layer structure predicted by the model were compared with CT-scans of the cells to assess performance. The genetic algorithm was found to be effective in converging the predicted wave response to the reference signal and creating accurate battery structures. It was shown that only part of the waveform was required to generate accurate predictions, which is helpful in avoiding parts of the signal contaminated by near field transducer effects.

It was demonstrated that the genetic algorithm can predict material wave speed to 40-1100 m/s (3-29 %) accuracy when battery layer geometry is provided; and thicknesses to within approximately 0.02-7.5 μm (1-13 %) when material properties are provided. Providing the genetic algorithm with parameter constraints; either the layer topology and/or the material properties, substantially improved predictions to estimate the wave speeds on average to approximately +/- 50 m/s (3-4 %) and the layer thicknesses +/- 5 μm (7-8 %).

This raises the possibility of the use of this approach to predict state of charge when the battery construction is known, or the presence of internal defects and damage to a known battery material composition.

Keywords

Lithium-ion battery, ultrasonic sensing, genetic algorithm, structure estimation

1. Introduction

There has been a substantial increase in the use of lithium-ion batteries in a range of applications, from handheld consumer technology to electric vehicles, since their introduction in the 1990's. This growth is expected to continue over the course of the next 10 years especially in the electric vehicle market [1]–[3]. To facilitate the safe, efficient, optimal usage of lithium-ion batteries, battery management (BMS) systems have been developed and employed. BMS have traditionally used external battery measuring methods such as coulomb counting, open-circuit voltage look-ups, and electrochemical impedance spectroscopy for battery reporting of state of health and state of charge [4]–[6]. More recently, non-invasive, real-time internal battery changes have been measured using ultrasonic pulse responses [7]–[10]. Piezo-electric transducers were used to generate ultrasonic pulses that partially reflected and transmitted at the different layers within the battery. The recorded wave amplitude variation with time, known as an A-scan, is a composite of these internal reflections (or transmissions). The changes in wave response have been found to correlate with battery state of charge (SoC) and state of health (SoH) [11]. There is good progress in this growing area of battery monitoring research, including spatially resolved measurements [12], defect detection [13]–[15] and real time degradation monitoring [16]. However, due to the large number of layers contained in lithium-ion cells [17], gaining deeper insights from ultrasonic wave responses remains challenging.

Genetic algorithms (GA) have been used in battery monitoring research previously where combinations of genetic algorithms and multivariate regression accurately estimate and model the State of Charge in Electric Vehicles [18]. In ultrasound, genetic algorithms have been employed in solving inverse problems in tomographic reconstruction, using time-of-flight data from ultrasound transmissions [19] and genetic algorithms have been utilised for processing and analysing ultrasonic signals obtained during thickness measurement, primarily in oil duct inspections, with the aim to accurately identify ultrasonic echoes for precise thickness measurements and detection of flaws such as cracks and corrosion [20]. Ultrasonic sensing of lithium-ion pouch cells has been combined with data fusion analysis [21], and ultrasonic analysis and machine learning techniques have been applied to predict state of charge and health of batteries [22]. However, no study has been found that employs genetic algorithm to gain insights from ultrasound responses in order to assess the internal structure of a lithium-ion cell.

In this work, a genetic algorithm has been constructed with the aim of using a cropped section of a single ultrasonic wave response to determine the component cell layers that would create that reference signal. In this way the internal structure of a cell can be reverse engineered from an ultrasonic reflection and transmission signal. This approach could then potentially be used to identify cell structure, charge, defects, or damage from easily measured ultrasonic signals. It was reasoned that genetic algorithms, with their inherent ability to search across a large, complex solution space, would be particularly well-suited for this task. The potential complexities and non-linearities involved in the wave response of a lithium-ion cell are unsuited to deterministic methods, while a genetic algorithm can explore and adapt to these complexities over multiple iterations. The choice was further motivated by the algorithm's robustness to local minima. The successful application of the approach, as

demonstrated by the results, vindicates this choice, and supports the continued use of such evolutionary computation techniques for similar challenges in the future.

2. Background

A wave incident at an interface between two bodies will cause some portion of the wave to transmit through the boundary with the remaining wave energy reflected. Each time this occurs, a new wave is created which subsequently travels through the body, encountering further interfaces according to the same rules. Taking measurements from an ultrasound response through a multi-layered lithium-ion battery is challenging due to the super-position of individual wave components; there is little physical insight available from individual reflections in an A-scan [17]. These theoretical challenges associated with ultrasonic monitoring of batteries are described in this section.

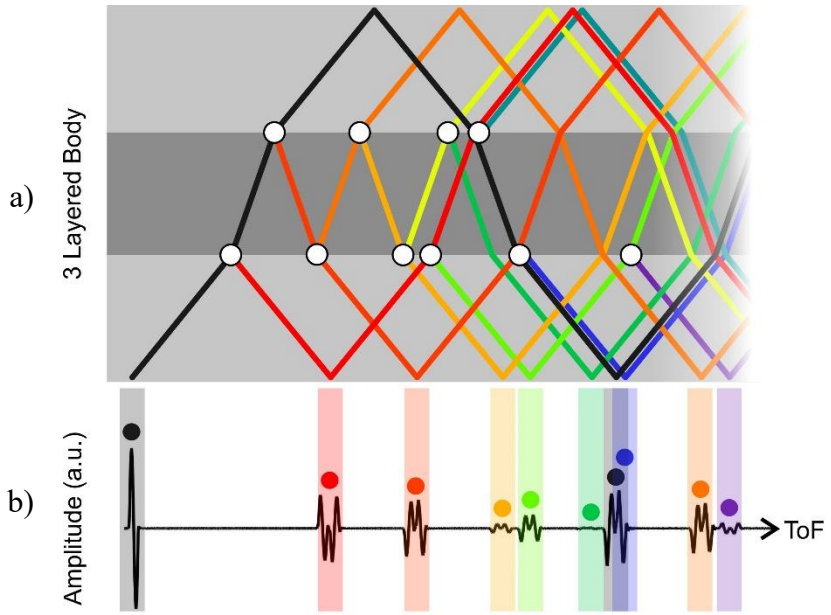

Figure 1: a) Schematic of waves travelling through a 3-layered body. Nodes indicate reflection/transmission events at each interface generating new wave paths. Waves all travel normally through the body – in the schematic the x-axis is the time of travel. b) An A-scan showing accumulation of the wave paths into a series of reflections. Peaks are colour coded according to the path followed.

Figure 1a shows the evolution of waves travelling through a simple 3-layered body. Nodes are marked at each location where the signal transmits and reflects creating a new wave path. The proportion of the wave amplitude reflected at each interface is described by a reflection coefficient *R*. Reflection coefficient depends on the acoustic impedance mismatch between the two materials according to;

$$R = \frac{z_2 - z_1}{z_2 + z_1} \qquad \text{Eq. 1}$$

Where z_n is the acoustic impedance of the material $z_n = (\rho_n\, c_n)$, ρ being the material density and c being the sound velocity for the material. The reflection coefficient R varies between 0 and 1 and the transmission coefficient, T is 1-R.

As lithium-ions pass between anode and cathode during charge cycling, the material density will change. This has two effects, firstly changing the acoustic impedance mismatch and

hence wave reflection; and secondly changing the speed of sound and hence time of flight through the battery.

When a single pulse is generated and the reflections are received, multiple reflections are associated with each layer, Figure 1b shows the received A-scan from pulsing through the 3-layered body. The peaks are colour coded to show the origin of each peak in the wave response. In this highly simplified construction, the A-scan quickly produced reflections that would be difficult to attribute to any one specific layer with certainty.

A lithium-ion battery is a multi-layer construction, consisting of multiples of anode, cathode and separator layers, each of which is referred to in this work as a 'unit cell', see Figure 2. The cell size depends on the number of unit cells contained in a battery and will relate to the battery capacity. This raises two important issues, firstly, the dimensions of the layers themselves becomes an issue, with waves spanning multiple layers, the subject of discussion in the section 2.1. Secondly, the number of layers creates a complex and chaotic wave environment and quickly becomes difficult to identify wave paths from A-scans, this is discussed in section 2.2. Note here that the battery construction is defined in terms of a cell during discharge, without reference to charge cycling in this work. These definitions are consistent throughout.

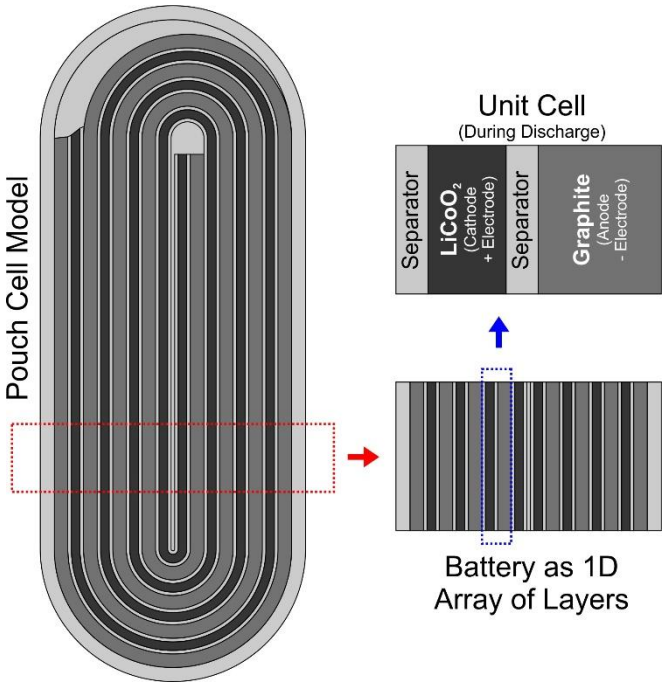

Figure 2: Schematic showing the roll construction inside a typical pouch cell. The roll creates multiple layers through which the sound wave will pass (here modelled as an 1D array). A single assembly of separator, cathode, separator, anode is here termed the 'unit cell'.

2.1. Partial Reflections

In current literature on the ultrasound monitoring of lithium-ion batteries many studies use sensors/pulse frequencies between 2 MHz and 2.5 MHz [7], [16], [17], [23]–[26]. With layer thicknesses in a battery cell approximately 25-100 μm, the wavelength (λ) from these frequencies will span multiple layers at once travelling through the cell. The wave travels through the cell and returns to the sensing edge with undefined characteristic responses as shown in Figure 3 (for illustrative purposes this figure has been created using wave

propagation modelling through a layered body described in Section 3.1). The response from the pulsed sine waves (red box) reaching the far side of the cell may be detectable (magenta box), however a collection of undefined peaks is also found in the green boxed region in this instance.

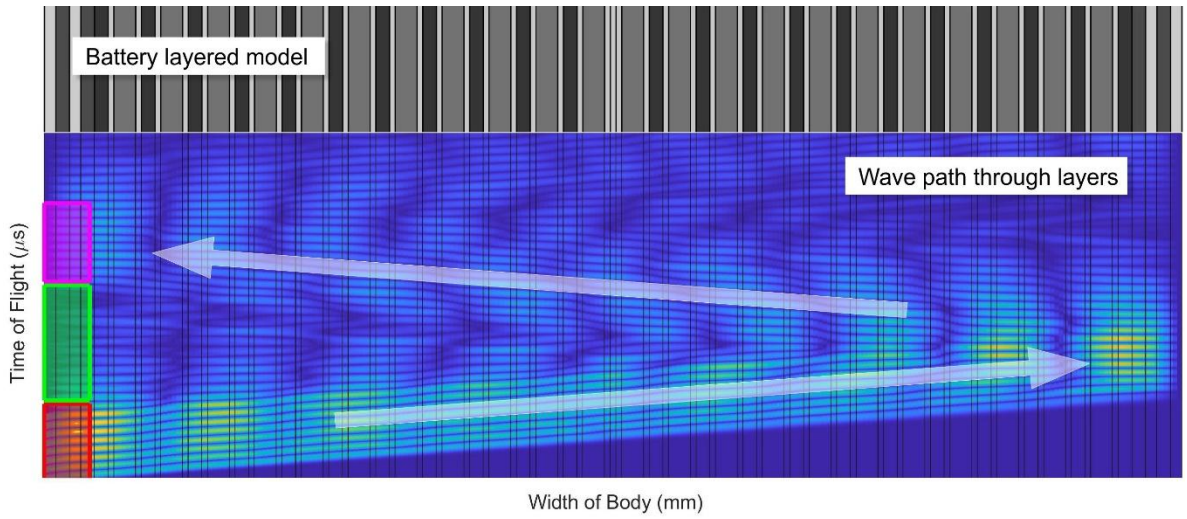

a)

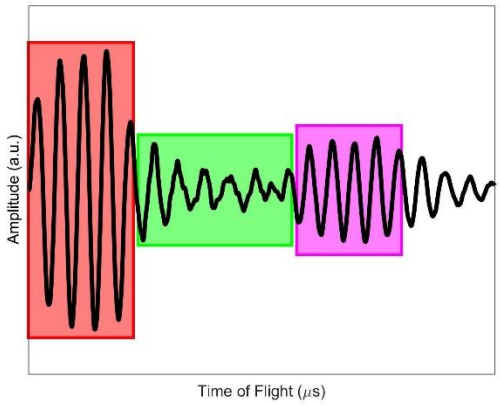

b)

Figure 3: a) Pulse/echo path taken through a model multi-layered cell. Transmitted waves (shown in the red box) and the 'reflections' from the far side of the cell (magenta box) are highlighted, undefined accumulated received signal is highlighted in the green box, b) A-scan showing the pulse/echo regions in red/magenta boxes and undefined accumulated signal in the green box.

Waves have a more complex relationship with material interfaces where the waves span multiple layers. In a layered system where the wavelength is shorter than a single layer thickness there will be clear reflected and transmitted sine waves. Whilst in the case where wavelengths span multiple layers partial reflections 'alter' the waves as they pass through layers. This continual misshaping occurs and compounds throughout the journey of the waves. All these partial reflections superimpose to form a complex pattern that is difficult to interpret.

2.2. Accumulated Constructive/Deconstructive Interference

The creation of new waves at each interface causes rapid escalation in signal response complexity, even with a few layers. This is demonstrated in Figure 4 which shows a six-layer

body, for simplicity, each layer is of equal thickness. Each node shows the possible pathways a wave would take to reach that point. The values along the left-hand edge (the sensing edge during pulse/echo, single sensor configuration) are of particular interest. In fact, the sequence formed along this edge is known as the *Catalan numbers*. This number sequence provides a solution to many counting problem applications, such as polygon triangulation, binary trees, and multiplication ordering [27], [28]. In this case the chaotic extent of constructive and deconstructive signal interference can be described using the formula

$$p_l = \frac{(2l)!}{l!\,(l+1)!} \qquad \text{Eq. 2}$$

Where p is the total number of pathways taken through all transmission/reflection routes to gain a 'full reflection' from an opposing face in pulse/echo configuration, through l number of layers. The accumulation of partial reflections prior to a full reflection form in the signal response, their features are difficult to interpret and can obscure the location of the full reflection. Summing these features along the sensing edge show the return of 196 unique wave paths through these 6 layers.

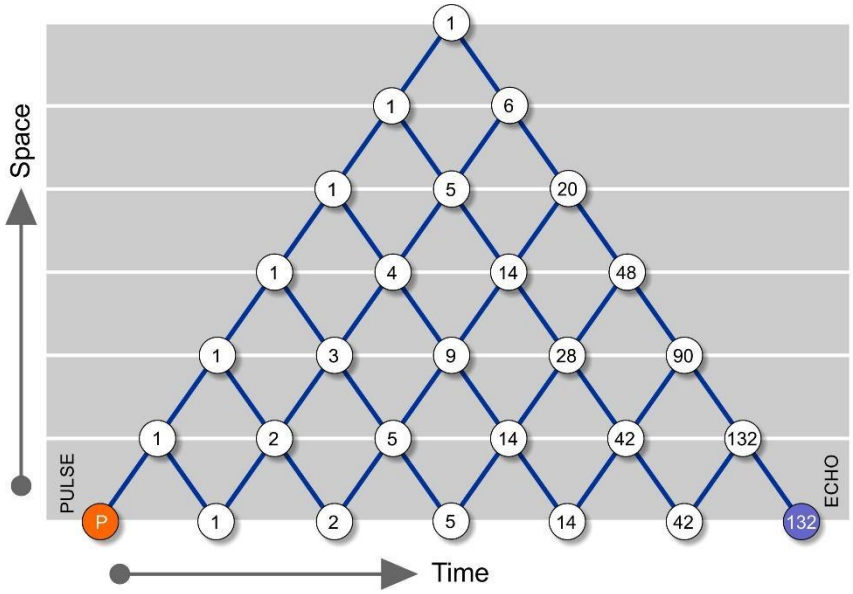

Figure 4: Accumulation of partial transmissions/reflections as an incident pulse travels through a six-layered body. Each node shows the number of paths that will arrive at that point with varying degrees of strength.

In previous battery modelling [17], to simulate a typical lithium-ion cell, approximately 20 unit cells (anode-separator-cathode) were defined. Each unit cell has 4 boundaries giving a body with at least 80 layers. Using Equation 2 the full reflection through an 80 layered body would contain the accumulation of approximately 1.13×10^{45} wave paths.

Further, to estimate the permutations of layer properties, assume the material wave speeds of the three component parts of a unit cell can range from 500 m/s to 6000 m/s, rounded to the nearest 100 m/s for simplicity. The thickness of each layer can range from 50µm to 100µm rounded to the nearest 5 µm. Half the number of active layers can range from 5 to 10 with a repeat of this around the centre space. Giving 11^3 x 56^3 x 5 ~ 1.17 x 10^9 permutations.

There are therefore two difficulties when interpreting acoustic responses when the waves cross many layers whilst travelling through the battery cell. Firstly, even if differences

between cells, or the same cell in different states (e.g. charge or health) are very minor and localised, the chaotic nature of the wave response would cause the small change to be difficult if not impossible to interpret – the *butterfly effect*. The second problem is the vast scope for layer property differences in a closed system such as a lithium-ion battery cell. Without knowing the exact material properties of all layers contained within the cell, predicting, and evaluating an ultrasound wave response is problematic.

2.3. Use of Chaotic Accumulation of Partial Waves in GA Estimation

Considering the above, it is evident that the signal response, particularly in pulse/echo sensor configuration, produces a waveform with subtle features specific to the precise layered structure under inspection. This paper suggests a method to use this chaotic and unpredictable nature of the wave response to reverse engineer the signal into the properties of the layers contained within a battery cell.

A heuristic approach to this problem is considered, providing approximations and estimations rather than the perfect solution. Metaheuristics are a set of intelligent strategies designed to enhance the efficiency of approximation techniques when dealing with larger scale, combinatorial, non-linear optimisation problems [29]. One such example is the genetic algorithm (GA), which is a nature inspired, population-based metaheuristic algorithm where the fittest solutions pass information to subsequent generations [30]. GA's are commonly used to solve complex problems from a range of fields such as; scheduling, forecasting, image/video processing, medical imaging, and engineering [31].

3. Algorithm Construction

3.1. Multi-Layer Acoustic Reflection Model

The algorithm is based on the multi-layer cell acoustic reflection model, developed in previous work [17], which follows from similar models in engineering acoustics [32]–[34]. The model predicts the passage of a wave perturbation through the layered body, based on a finite difference solution to the 1D wave partial differential equation:

$$u_{tt} = c^2 u_{xx} \qquad \text{Eq. 3}$$

Where u is the wave position in space x and time t. The wave speed c is applied as an array of values simulating the material wave speed in each layer. The differences in speed values between nodes provide the material interfaces from which reflection and transmission events occur.

Simulated ultrasound pulses are transmitted through the candidate layers to retrieve the wave response provided for that cell estimation. Figure 5 shows a typical modelled cell and the resulting output. In the left-hand picture, an array of 22 unit cells is constructed; the greyscale shows the variation in material wave speed, due to variations in density and elasticity in each layer material. The right-hand side shows the simulated A-scan wave response from the modelled cell.

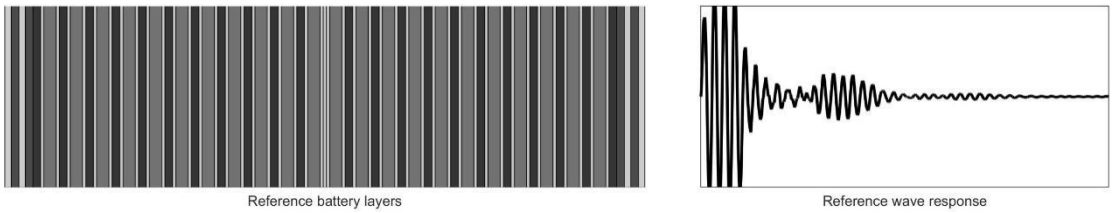

Figure 5: (Left) Battery cell modelled layers, greyscale represents material wave speed, layer thickness drawn to scale. (Right) Predicted pulse/echo wave response from these modelled battery layers. (Black waves are used throughout to represent a reference wave).

The GA is designed to predict a layered structure that generates a wave response that is matched to this reference signal. Initially, the GA is tested using this model-model method. In theory, at least, the wave can be fully matched and therefore exact layers can be found. Later, the GA is used to predict the layered structure associated with an experimentally measured single ultrasound wave response from a commercial lithium-ion pouch cell. Applying this method to experimentally obtained cells is limited to the quality of available modelling techniques. The GA is model independent, the A-scan generation from layered properties can be obtained by any means to help improve accuracy.

3.2. Genetic Algorithm Structure

A flow chart of the GA construction is shown in Figure 6. An initial random guess of the 1D layered battery structure is made, constructed according to rules set out to simulate a lithium-ion battery cell as described in Figure 2. In section 4 we explore how starting with some predefined parameters affects the solution.

A population of mutations is created, and the model of section 3.1 used to predict the acoustic response of each mutation. The acoustic response from each candidate in the population is compared to the measured reference acoustic response, and the fittest chosen for propagation. The GA runs until either a threshold below which a solution is considered close enough is reached, or when an imposed time limit is exceeded.

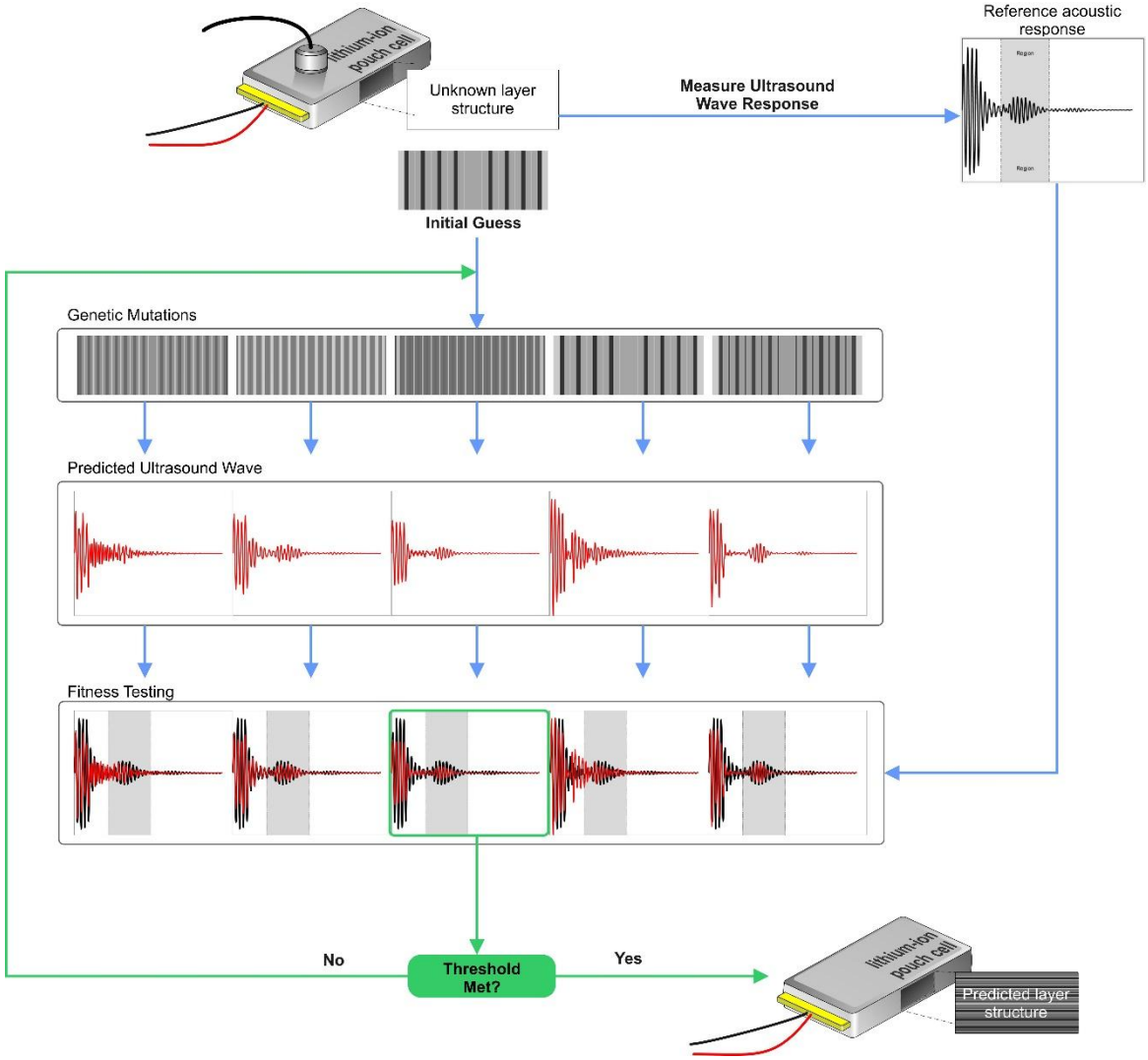

Figure 6: Genetic algorithm flow schematic. An initial guess at the cell layer structure is made; a population of mutations is created. The ultrasonic response of each mutation is predicted. Each predicted response is compared to the measured ultrasonic response. The fittest solution is chosen for propagation. (Red waves are used throughout to represent a latest match of the entire waveform).

3.3. Mutation Rules

The mutation rules form one of the most important parts of the GA, shown graphically in Figure 7. The basis of the cell construction for each candidate follows the same structure:

{casing : *n*(unit cells) : central separator : *n*(unit cells [mirrored]) : casing [mirrored]}

Where *n* is the number of *unit cells* where each unit cell is comprised of (cathode-separator-anode-separator) as shown in Figure 2. There are five methods of mutation, denoted M1 through to M5, each of which occur at the specified mutation rates.

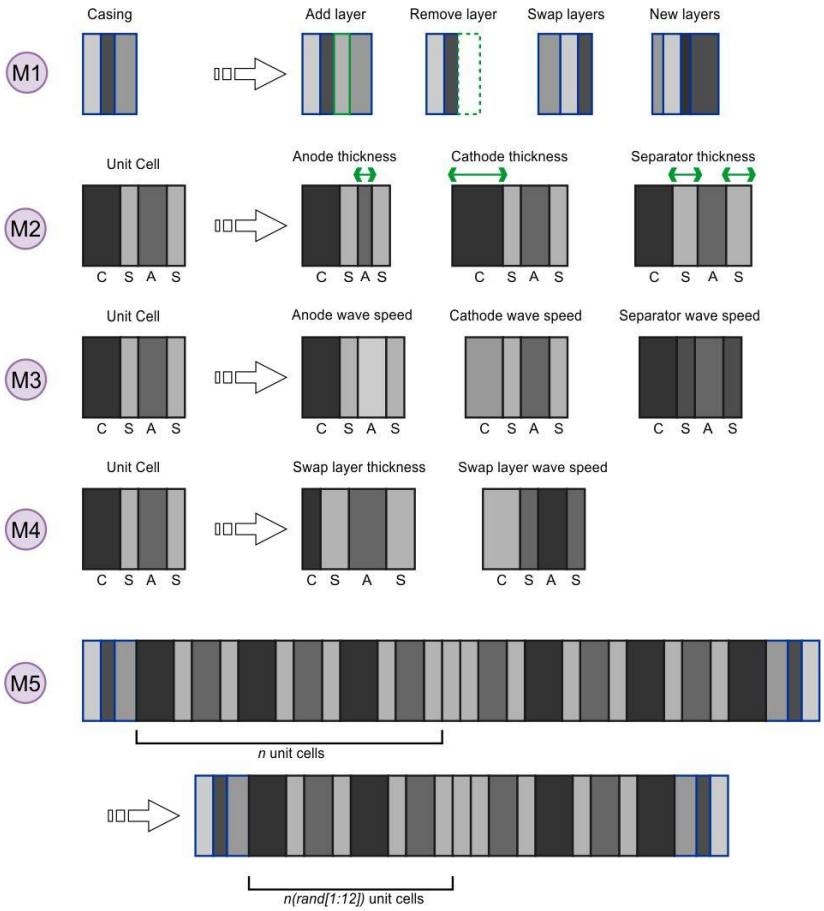

Figure 7: Schematic diagram of the five mutation rules used to generate a new population.

M1. In this strand one of the following mutations can occur in the casing layers:
   a. An additional layer is inserted in a randomised position.
   b. A random layer is removed.
   c. The ordering of layers is randomly swapped.
   d. A new randomised set of layer parameters (number of layers, wave speed, thickness) is generated.

M2. In the unit cell, the thickness of one of the layer types can be randomly altered.

M3. In the unit cell, the wave speed of one of the layer types can be randomly altered.

M4. The ordering of thickness or wave speed parameters can be swapped randomly.

M5. The number of units cells can be changed to a new random value.

The rules for these mutation events occur according to chance for each candidate at each generation.

3.4. Fitness Testing - Wave Matching

For the GA to work, a suitable fitness test must be applied to each candidate to determine which waveform is most closely matched to the reference signal. There are three main steps to ensure the best matched candidate is chosen, such that the fittest layer parameters can form the basis for the next generation. Figure 8 shows a selection of sample candidates together with some illustrations of measuring methods. In each case the reference signal is displayed in black, whilst a candidate waveform is shown in green.

1. **Correlation** was used to compare the likeness of two signals. In the example shown in Figure 8a, for candidate 1 a strong relationship is evident by visual inspection, although the two signals are slightly out of phase. Compare this to the waveform of candidate 2 in Figure 8c, where the reference and candidate signals are closely matched in phase. The waveform of candidate 3 is shown in Figure 8d, here the signal is anti-phase with the reference.
2. **Dynamic time warping** (DTW) is a more robust method of measuring the similarity of two signals that have different phases or have common features out of sync [35], [36]. This forms the second fitness test for each candidate, an illustration of which is shown in Figure 8b. Notice the lines are not horizontal here, they match common signal features providing good matching measurements for signals slightly out of phase.
3. **Correlation symmetry** is where the correlation difference between the first and second half of the candidate waveform is measured. Ensuring that the signal has a good match with all parts of the reference rather than a strong partial relationship, the GA can mitigate the risk of becoming stuck in local optima. In Figure 8 the red lines measure the correlation for the first half, blue lines for the second. This process is only completed for the correlation tests, as such the measuring line approximations are shown as grey for the DTW in Figure 8b.

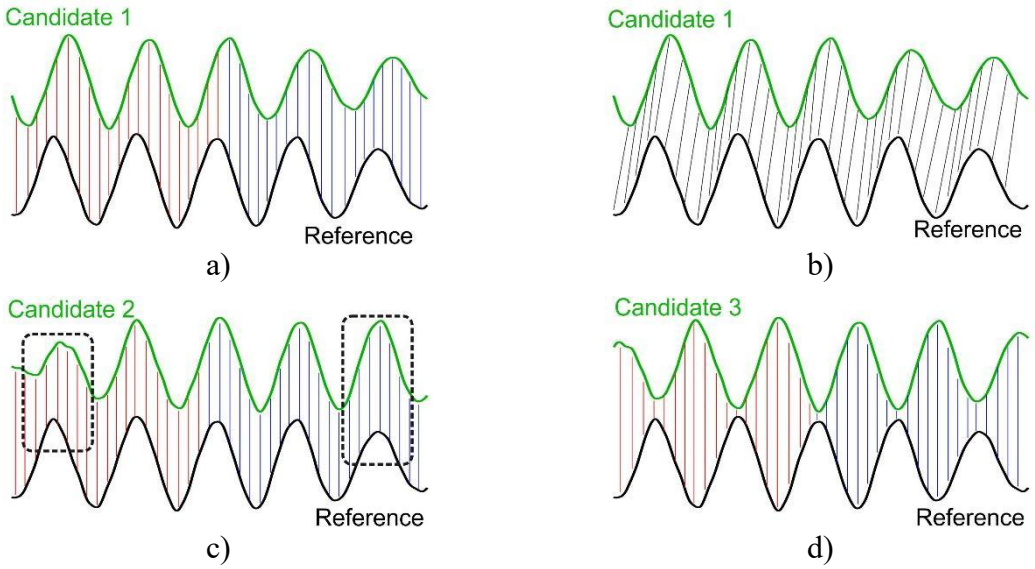

Figure 8: Search regions from three candidates (green) compared with reference signal (black). a) Correlation when out of phase, b) dynamic time warping when out of phase, c) unbalanced correlation, in phase with, d) anti-phase correlation. (Green waves are used throughout to represent the latest match of the search region).

In this instance, the layer parameters that created the waveform of candidate 2, the fittest candidate, would be passed to the next generation as the basis for the new population. The mutation and selection of the fittest candidate will repeat until the fitness rating value drops below the set threshold, or the GA is timed out.

3.5. Monitoring GA Progress

This section demonstrates how the GA attempts to estimate the reference cell structure shown at the top of Figure 3 and monitor its performance at each iteration. The plots in Figure 9 track the layer parameters of the fittest candidate of each generation. Figure 9a shows the number of unit cells (green) in half of the cell (mirrored around the centre winding space). The colour coded dots on the right-hand axis are pinned at the value producing the best solution found by the GA.

Figure 9b shows the predicted wave speeds for anode, cathode, separator, and casing. Figure 9c shows the predicted layer thickness for each component. Together these plots show the layer parameters for the fittest candidate selection at each generation.

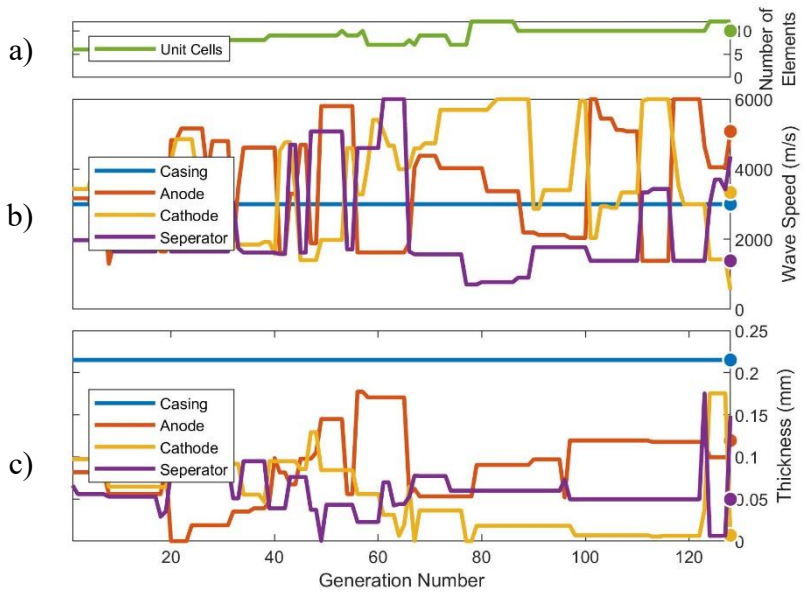

Figure 9: Live search parameters, (a) number of unit cells predicted (b) wave speed of components and (c) thickness of individual layers.

The changes driving the GA finding better solutions are based in the fitness testing part of the GA. Each time a new best solution is found, the candidate signal is plotted against the reference for direct comparison. In Figure 10a the fittest match from an early generation is displayed; this is the best solution found at that point. The top panel shows the selected search region, subjected to the fitness testing, whilst the bottom panel shows the whole signal length with the search region shaded in grey.

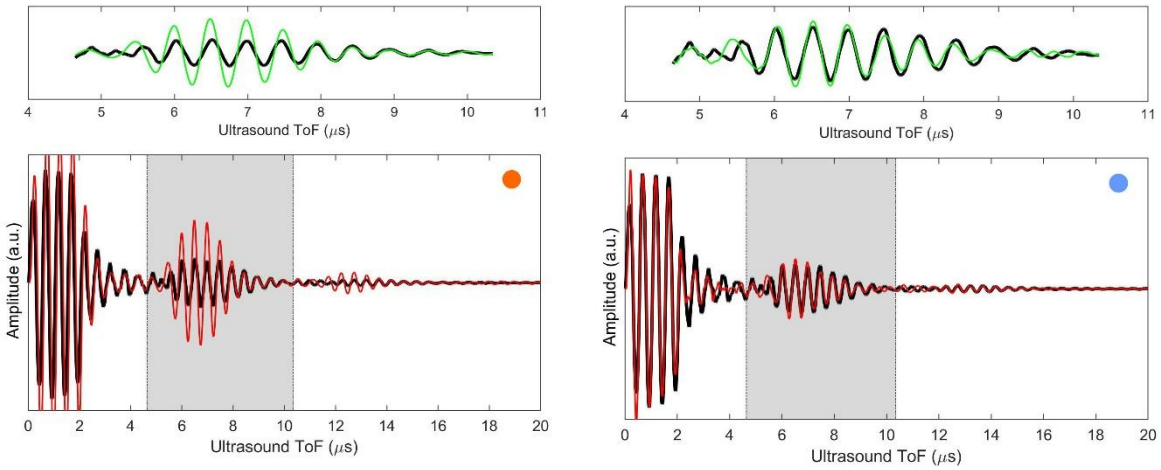

Figure 10: Best match plots, black plot is the reference signal, green is search region best match, red is full wave response match, a) early test best match and b) late test best match.

The match is clearly better by the later generation (Figure 10b) with the green and red lines of the candidate waveform closely resembling the reference. Interestingly, as the solution converges around the search region, so does the entire waveform around the reference signal. This adds weight to the argument that a small sample of the signal contains precise details about the specific layer construction of a cell. This is a useful finding if this GA wishes to avoid unwanted artefacts in the ultrasonic signal such as transducer ring-down, which can occur in the early part of a signal.

A GA progression *dashboard* is presented in Figure 11. This visually demonstrates the evolution of the predicted cell structure as its waveform increasingly aligns with the reference signal. The red horizontal line, shown across the bottom panels of the dashboard, marks the generation of the last, best found solution and corresponds with the graphical prediction, component wave speed, number of layers, and layer thickness for that prediction.

The success of the GA is measured in the bottom right corner of the dashboard. The blue line shows GA threshold tracking and should converge to the dotted line on the left, while the orange line shows the correlation for the full wave response with the reference, ideally trending towards 1 on the right. The learned layer progression is displayed in the top left corner of the dashboard, where common layer dimensions are collated and shown. The wave response for the search region and full response signal for the last best solution are compared with the reference in the centre and right side of the top panel of the dashboard.

Videos of shortened sequences of the GA progression dashboard are included in the supplementary material which help visualise context and development of each panel.

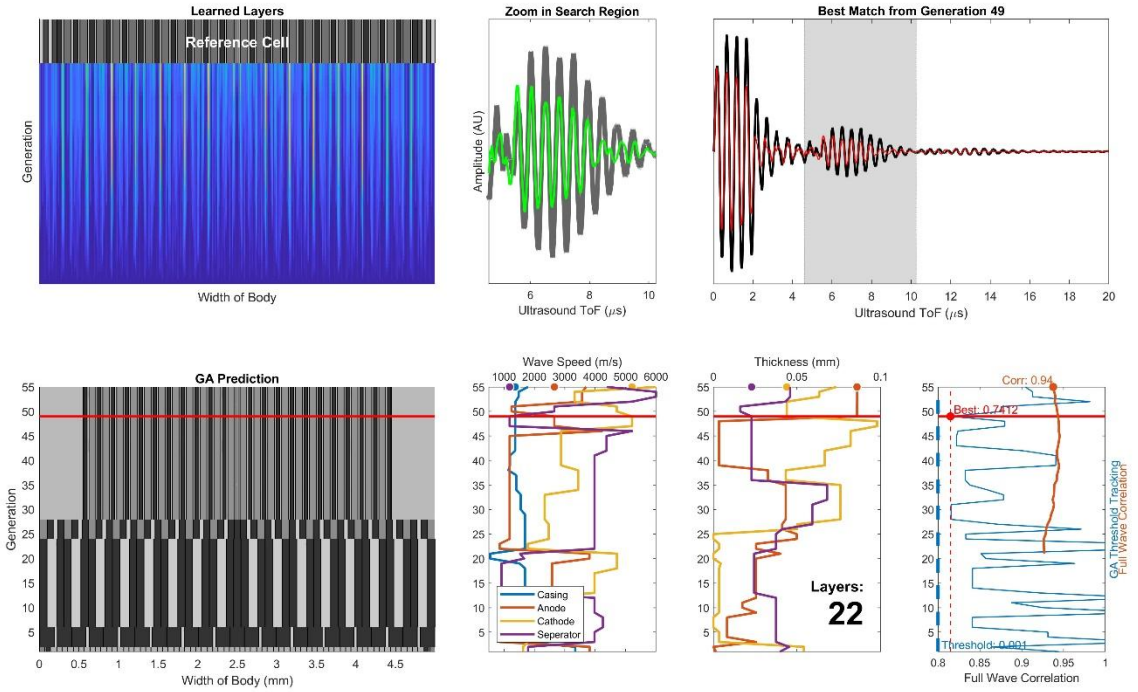

Figure 11: Dashboard for GA progression. Top panel left to right: 'Learned layer' development, search region best match/reference and full wave best match/reference comparison. Bottom panel left to right: Battery layer graphical prediction development, wave speed and thickness predictions for each generation, GA metric tracking (the blue line is an arbitrary wave matching parameter and full wave correlation).

As the solution evolves from generation to generation, it is not necessarily the case that a new mutated population retains all the fittest aspects of the structure. A certain aspect of a solution (e.g., separator location and thickness) might repeatedly appear in an early generation and then not in later generations. It is useful to track where the same aspects of a structure are repeatedly observed appearing in multiple generations; these are denoted 'learned layers'.

The location (i.e. the x-coordinate – distance from the battery left edge) of each layer boundary is recorded at each generation. These boundary positions are sorted into set bin widths to uniformly accumulate the data. The dashboard in Figure 11 shows a snapshot of the learned layers. The animated videos in the supplementary materials show more clearly the accumulation of the layer information.

4. Parameter Overrides

In practical application it is reasonable to assume that some battery parameters would be known or at least closely estimated prior to commencing a search. The initial conditions can therefore be set overriding some of the cell parameters; casing, anode, cathode and separator layer thicknesses and wave speeds, casing layers and number of unit cells. The override can be performed by reducing the search range, for example, without an override an anode would have a material wave speed range of 500-6000 m/s, this could be altered to 4000-4500 m/s.

In these test cases two overrides are evaluated:

(a) Known battery geometry. All parameters apart from the material wave speed of each layer are set precisely according to the reference object. The GA is then searching to determine the wave speed for the cathode, anode, and separator layers only. This could, for example, be used as an approach for determining the state of charge of the battery, since the charge will change the density and hence wave speed in the electrode layers.

(b) Known layer properties. Wave speeds for each layer material are input to the GA as constants, leaving the algorithm to search for the layer dimensions and battery geometry. This could, for example, be used to detect geometric irregularity during manufacture or damage to the battery structure.

Figure 12 shows the results for each of these two cases. For the known geometry case there is almost no noticeable discrepancy in the predicted wave form (Figure 12a). All features now match closely in the search region and in the full signal match. This further reinforces the assumption that the subtle features of a signal response are unique to the specific layer structure under inspection. The shading/wave speeds for all unit cells is estimated with very high accuracy (Figure 12c). It would be expected that allowing longer search times using a stricter accuracy threshold value would give the GA an opportunity to refine the search even further.

For the known battery materials case (Figure 12b), again the GA closely matches with the predicted wave response to the reference. The predicted battery geometry matches well with the modelled reference cell, the dimensions are accurate, and the number of layers is well defined as shown in the graphical comparison in Figure 12d.

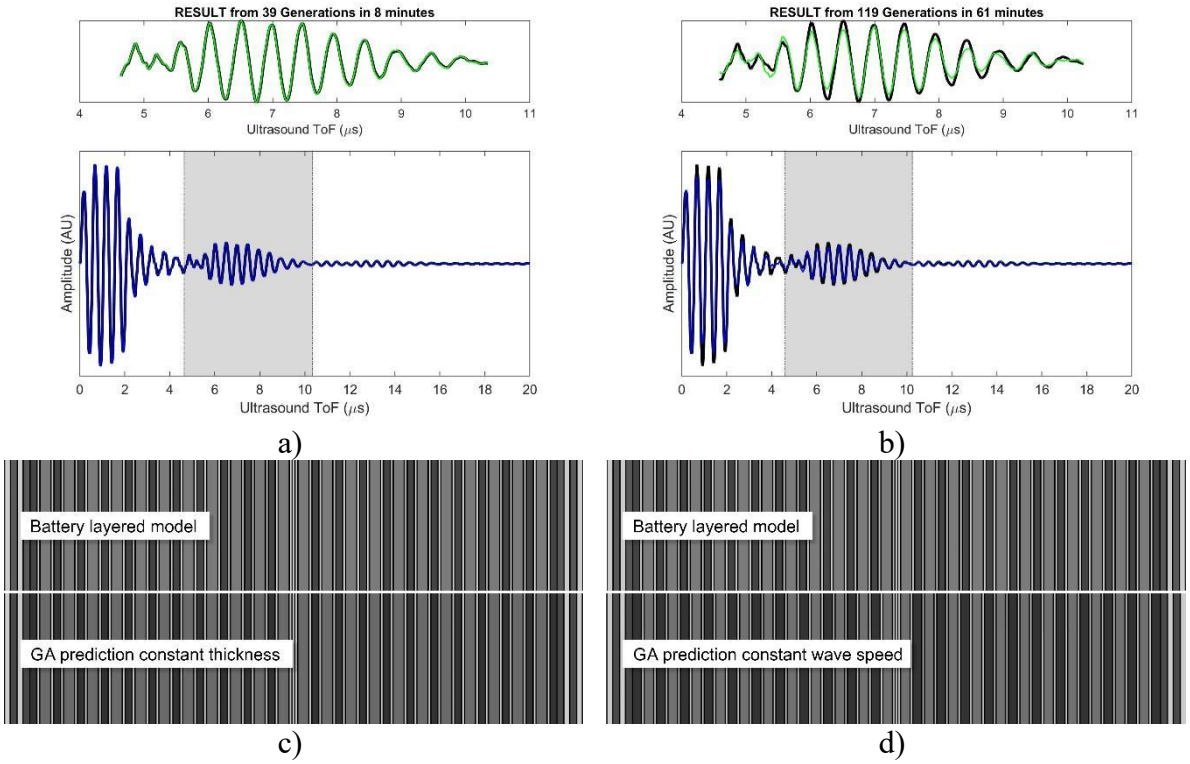

Figure 12: Best match plots using overrides, a) early test best match, b) found solution match and c) GA estimation synchronised with sample cell parameters from modelling. (Blue waves are used to represent a final GA prediction once stopping conditions are reached).

5. GA Testing on Modelled Reference Battery

In this section a model-model comparison has been conducted. A reference cell layer structure was created, and the reflection model used to generate the associated reference waveform (the actual layer structure and the waveform are shown in Figure 5). The GA was then used to generate a predicted layer structure based on the waveform matched to the reference waveform.

Performance of the GA can be monitored in two ways; the success of wave matching, and the quality of the battery cell layer estimation compared to the reference object. Both are described in this section.

5.1. Evaluation: Wave Matching

The plots previously shown in Figures 10 a&b demonstrate the evolution of the waveform and the matching progress throughout the generations. Where the reference signal is plotted in black, and the latest best match is overlaid in red. Here it is shown that the later wave more closely matches the reference. The dashboard in Figure 11 (top right panel) shows the latest best match. Particularly viewing the animated search sequences in the supplementary material, the convergence of the GA predicted wave response to the reference wave is clear.

The dashboard plot in Figure 11 (bottom right panel) also shows the tracking of the GA progression metrics. The key metric driving the search is the wave match fitness testing which produces a value which aims to be closer to the low threshold. Whilst there is some erraticism in the search the trend is towards the threshold as the GA successfully converges the search region to the reference. In addition, the correlation of the full predicted wave response with the reference wave is monitored, it would be hoped that as the search region converges, the correlation will improve or stabilise. This is seen in the dashboard.

4.2. Evaluation: Battery Layer Prediction

Table 1 shows the numerical results from GA searches for four different starting conditions:

- Test 1 - a ‘free’ search in which no known or estimated values are predefined.
- Test 2 - a ‘thickness’ search where the material properties and number of layers are predefined.
- Test 3 - a ‘material properties’ (wave speed) search where the number and thickness of all components is predefined.
- Test 4 - a ‘constrained’ search where the possible range of wave speed and thickness values is constrained to within predefined limits.

	Location from battery front edge (mm)		Material Properties Wave Speed (m/s)			Component Thickness (μm)			Number of Layers, #
Parameter	Casing Position	Centre Space Position	Anode	Cathode	Separator	Anode	Cathode	Separator	
Reference									
True Value	0.2201	2.4625	3800	5700	1128	96.0	60.0	25.0	22
TEST 1: Free Search									
Prediction	0.1537	2.4091	1046	4366	5573	40.8	48.4	60.6	22
Error (+/-)	0.0664	0.0534	2754	1334	4445	55.2	11.6	35.6	0

Error (%)	30.2	2.2	72.5	23.4	394.1	57.5	19.3	142.4	0
TEST 2: Thickness Search (casing, speed, and layer overrides)									
Prediction	0.2303	2.4628	3800	5700	1128	103.3	52.2	24.8	22
Error (+/-)	0.0102	0.0003	-	-	-	7.3	7.8	0.2	-
Error (%)	4.6	0.0	-	-	-	7.6	13.0	0.8	-
TEST 3: Wave Speed Search (casing, thickness, and layer overrides)									
Prediction	0.2196	2.4628	4905	6000	1090	96.0	60.0	25.0	22
Error (+/-)	0.0005	0.0003	1105	300	38	-	-	-	-
Error (%)	0.2	0.0	29.1	5.3	3.4	-	-	-	-
TEST 4: Constrained Search (Speed: +/- 500 m/s of known, Thickness: +/- 15 µm of known)									
Prediction	0.2110	2.4641	3802	5698	1020	91.0	68.0	24.0	22
Error (+/-)	0.0091	0.0016	2	2	108	5.0	8.0	1.0	0
Error (%)	4.1	0.1	0.1	0.0	9.6	5.2	13.3	4.0	0

Table 1: Predictions of the GA for four test cases with differing pre-loaded initial conditions. The results shown are predictions of; location of two battery components, wave speeds of the layer materials, thickness and number of layers. The prediction accuracy in each case is shown. Cells highlighted in orange have been pre-loaded into the GA and held constant. Cells highlighted in green have been constrained to lie within predefined limits.

The results show that the GA is capable of making a highly accurate representation of the cell when constraints are applied to the search. In the case of a completely free search, whilst accuracy is greatly reduced, it is worth noting that when inspecting the graphical comparison (Figure 13) of the GA and reference geometries, some resemblance is still apparent.

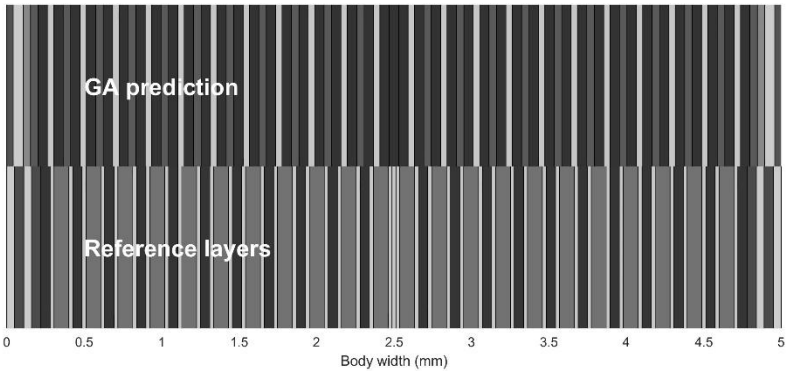

Figure 13: GA prediction compared to reference layers from a free search case.

A constrained search, where the parameters have predefined ranges around the known value, yield better results. This search can estimate the wave speed, on average to approximately +/- 50 m/s (3-4 %) and the layer thickness +/- 5 µm (7-8 %). When overrides are used and some parameters are considered known values and the GA is tasked to find the unknown parameters, again the GA performs well and predicts the material wave speed to within approximately 40-1100 m/s (3-29 %) when thicknesses are provided and thicknesses to within approximately 0.2-7.5 µm (1-13 %) when wave speeds are provided. The searches covered in these results are typical of those obtained and are achieved with a 30 minute time limit for the GA search and a population of 100. Increased time and/or population would be expected to return superior results.

6. GA Testing on a Measured Battery

The GA was tested on experimentally obtained reference waveforms from two commercial lithium-ion pouch cells. Cell 1 was a RS Component 190 mAh cell model HPL402323-2C with dimensions 25 mm x 24 mm x 4.2 mm. Cell 2 was a Farnell 165 mAh model LP-402025-1S-3 with dimensions 26 mm x 20 mm x 3.8 mm.

6.1. CT Scan Data and Measured Ultrasonic Waveforms

CT scans of the internal structure of both cells were obtained. The CT-scans were conducted on a Zeiss Xradia 620 Versa X-ray microscope. The scan used a 4 × lens at 4 second exposure providing resolution with a pixel size of 3.89 µm.

For the ultrasound wave response acquisition, commercial longitudinal contact transducers were used to both transmit and receive an ultrasound pulse in a pulse/echo arrangement. The sensor was clamped in place and a high temperature ultrasound gel was used as a couplant. The sensor was connected to a PICOSCOPE 5000 Series oscilloscope which was used to generate the pulse and record the reflected waves. The pulse consisted of 3 sine waves at a frequency of 2 MHz, the response signal captured was 0-16 µs with a time resolution of 2-8 ns. Bespoke LabView software was used to control the PICOSCOPE in both signal generation and capturing the signal response. The response capture range was 0-16 µs with the cell charged to a nominal capacity. More details of the experimental procedure that was used to obtain the ultrasonic waveforms can be found in previous work [17].

Figure 14 shows the CT scan for the RS cell (Cell 1). The green square is a crop of the layer structure and is annotated to show the cathode with the aluminium (Al) current collector and the anode/separator with the copper (Cu) current collector. The separator itself is low density and is not clearly visible in this scan. The structure is marked according to the scans of similar nature by taken by Gelb for the ZIESS Xradia 520 Versa technical document on lithium-ion battery imaging [37].

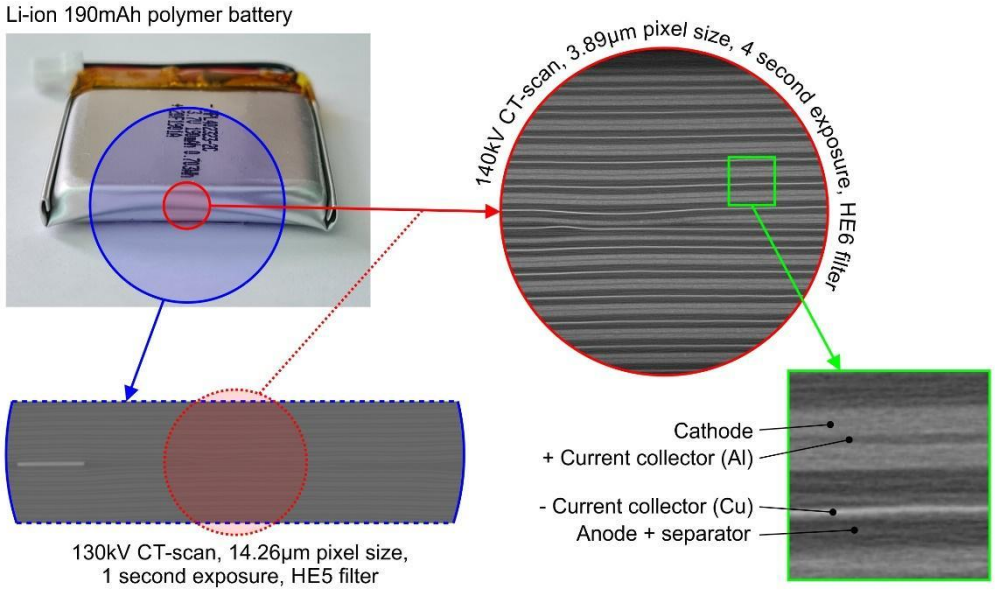

Figure 14: Two scans taken of the RS HPL402323-2C battery cell; low resolution 14.26µm pixel (blue) and high resolution 3.89µm pixel (red), crop of layers showing electrodes and current collectors (green).

The scanned layers from each of the cells in shown in Figure 15. To the right of the scans is a measured sample ultrasound waveform captured using 2 MHz pulses in a single sensor, pulse/echo configuration. These waveform responses were used as references for the GA to estimate the layer properties such that the output could be compared directly with CT scans.

The search region selected for each test is shown in the grey boxed region of the waveform in Figure 15. Setting the search region in this way avoids the ringdown region (i.e., the region close to the initial burst of the sensor where the piezo-electric element experiences some residual vibration after electrical oscillation has ceased).

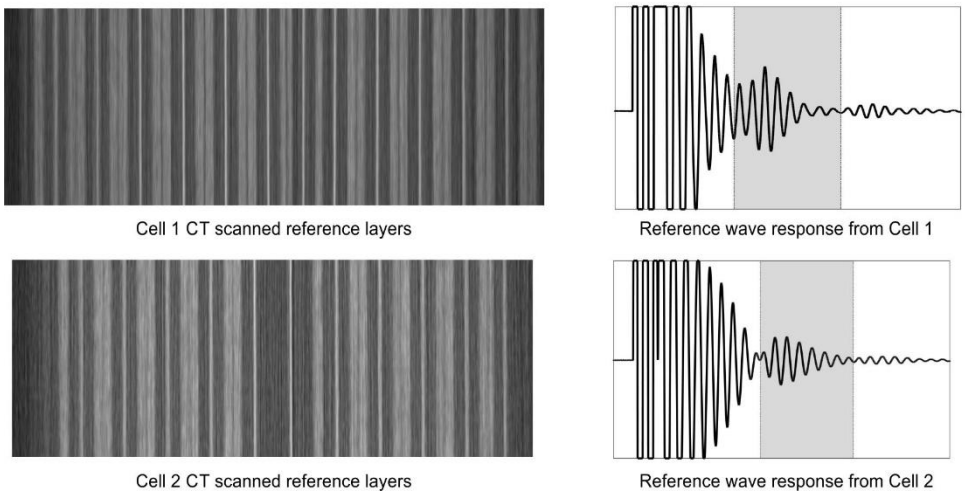

Figure 15: (Left) Battery cell reconstructed layers observed in the CT-scan. (Right) Measured pulse/echo wave response from scanned cell. The GA search region is shaded in grey.

6.2. Predicted Battery Structure

Having the CT scan data provides an opportunity to compare the scanned layers with the GA layer estimations, the results are shown in Figure 16. Looking firstly at the cell properties estimated by the GA in the lower half of the comparison. The number of unit cells is well estimated with 6 and 5 predicted in the half-battery, matching with the CT scans of Cells 1 and 2 respectively. Whilst the precise synchronisation of the unit cells is not accurate, the GA has made a good attempt at predicting the overall cell structure of each of the cells.

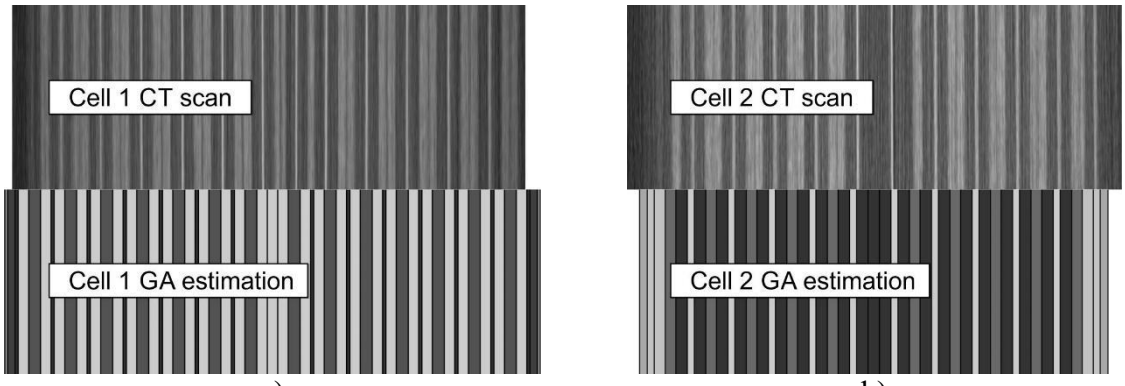

Figure 16: GA estimation synchronised with sample cell parameters from small capacity cell CT scan and learned layer boundaries for a) cell 1 and b) cell 2

It is important to note at this point that the GA is unable to find a perfect match with the CT scan. Principally, this is because the low density of the separator means it is hard to detect in the CT scan. This means that the repeating unit cell in the CT scan image is of the form:

{anode-current collector-anode-cathode-current collector-cathode}

Whilst the model is based on a repeating unit cell of the form:

{cathode-separator-anode-separator}

Changing the unit cell structure to [ABACDC] as opposed to [ABCB] would be desirable for future work. However, the assortment of diverse materials, current collectors that are typically made of dense aluminium (Al) and copper (Cu), porous electrodes with positive metal oxide and negative graphite components, and a separator would present distinct characteristics when evaluated via different methods, such as X-ray tomography and acoustic wave transport.

7. Discussion

In the present study, it was observed that during the (GA) operation, the parameters defining individual battery components did not converge to a single solution. Rather, they exhibited dynamic behaviour, scanning a broad parameter space and unveiling various combinations that effectively matched the resultant waveform to the reference wave derived from the examined cell. This behaviour might be attributed to the inherent complexity of the lithium-ion battery layered structure and the superposition of internal reflections.

An important result of this research did not lie in the convergence of individual parameters but in the convergence of a chosen region of the resulting ultrasound waveform response. Despite obstacles such as local optima, the GA successfully refined the waveform progressively, converging towards the reference wave.

Currently, the method lacks precision when performing a free search. The wave matching will converge closely around the reference, but the search is susceptible to getting trapped in local optima despite initial efforts to circumvent this. Although quantitatively less accurate, the graphical representation can mimic the reference cell, as shown in Figure 13 and important values such as the inner dimension of the casing and the size of the central space around which the layers wind are frequently well-defined. Attempts to use the method to measure state of charge were hindered by this lack of accuracy, being significantly greater than the material differences during charge states. Therefore, enhancing the precision of the method is vital to harness its potential for battery state measuring and defect detection.

The GA can swiftly generate accurate representations of the battery cell layers when using parameter overrides or constraining search values. If some prior component knowledge is provided to the GA, it can estimate the material properties and layer thicknesses with excellent accuracy. This possibility makes the GA method a potentially robust tool in ultrasonic battery monitoring and broader battery management systems. Additionally, the GA consistently identified certain true aspects about the layers, even with the potential for imperfect structure predictions. This ‘learned layer’ information could serve as valuable data for machine learning applications, contributing to future searches and potentially improving prediction accuracy and convergence speed.

In the test results presented in this study, a time limit of 30 minutes was set. During this period, approximately 80-100 generations occurred each with a population of 100 candidates. The algorithm consequently generates around 8000-10000 potential battery geometries, each with a distinct and precise set of parameters. Considering that an 80-layered body would

present approximately 1.17×10^9 permutations as discussed in section 2.2, this GA search is deemed well-guided and computationally cost-efficient.

8. Conclusions

This study proposes a novel and powerful method to extract rich information from a sealed lithium-ion cell. The only requirement is a single wave response to an ultrasound pulse sent through the battery. From this a small section of the wave can be selected as a search region, avoiding unwanted artefacts such as transducer ring down or signal attenuation.

A genetic algorithm has been built to harness the complexity of battery structures of unknown layers, dimension, and material properties. Candidate battery structures were evaluated by predicting the ultrasonic response using a numerical wave propagation model. This predicted wave response was compared to the measured response to select the fittest candidates. The iterative passing of generations allowed the search to find wave responses that matched ever more closely during test progression.

The GA has been evaluated in two ways; firstly, by requiring it to predict a known idealised model battery structure with its predicted waveform (a model-model comparison), and secondly, by using a measured ultrasonic waveform from a pouch cell where the internal structure has been obtained by CT scan (a model-experiment comparison). In all cases the GA worked well to predict the internal structures.

The GA was evaluated on test cases where no prior knowledge of the internal structure was provided. In practical application it is likely that some information will be known (for example the number of layers and the unit cell topology, or the material properties of the components). Where extra information was used as model input, the GA performance improved substantially, and almost perfect predictions were achieved. The study illustrated that, given the material thicknesses, the genetic algorithm can approximate the speed of material waves with an accuracy of 40-1100 m/s (3-29 %), and with material properties provided, it can estimate thicknesses within roughly 0.2-7.5 μm (1-13 %).

The accuracy of the predictions significantly improved when constraints were applied to the genetic algorithm, either through the layer topology or the material properties. With these parameters in place, it was possible to estimate wave speeds with a precision of approximately +/- 50 m/s (3-4 %), and layer thicknesses to within +/- 5 μm (7-8 %). This raises the possibility of using the GA to predict the state of charge (as this affects the electrode properties), or the presence of damage or defects (as this changes the layer structure).

9. Acknowledgments

RDJ would like to acknowledge the Engineering and Physical Sciences Research Council for funding this research through his fellowship on *Tribo-Acoustic Sensors* EP/N016483/1 and the Centre for Doctoral Training in Integrated Tribology EP/L01629X/1. RC would like to acknowledge the funding provided by the University of Sheffield and the EPSRC through the Knowledge Exchange Scholarship Scheme X/014525-12. RC would also like to thank Dr Ria Mitchell of the Sheffield Tomography Centre at the University of Sheffield for providing the CT scans of the lithium-ion batteries.

10. Declaration of Interest Statement

There were no conflicts of interest.

11. References

[1] L. Lu, X. Han, J. Li, J. Hua, and M. Ouyang, "A review on the key issues for lithium-ion battery management in electric vehicles," *J. Power Sources*, vol. 226, pp. 272–288, 2013, doi: 10.1016/j.jpowsour.2012.10.060.

[2] Bloomberg NEF, "Goodbye Gadgets," 2019. https://about.bnef.com/ (accessed Nov. 19, 2019).

[3] V. Ramadesigan, P. W. C. Northrop, S. De, S. Santhanagopalan, R. D. Braatz, and V. R. Subramanian, "Modeling and Simulation of Lithium-Ion Batteries from a Systems Engineering Perspective," *J. Electrochem. Soc.*, vol. 159, no. 3, pp. R31–R45, Jan. 2012, doi: 10.1149/2.018203jes.

[4] Y. Wang, J. Tian, Z. Sun, L. Wang, R. Xu, M. Li, and Z. Chen, "A comprehensive review of battery modeling and state estimation approaches for advanced battery management systems," *Renew. Sustain. Energy Rev.*, vol. 131, no. March, p. 110015, 2020, doi: 10.1016/j.rser.2020.110015.

[5] W.-Y. Chang, "The State of Charge Estimating Methods for Battery: A Review," *ISRN Appl. Math.*, vol. 2013, pp. 1–7, Jul. 2013, doi: 10.1155/2013/953792.

[6] M. Berecibar, I. Gandiaga, I. Villarreal, N. Omar, J. Van Mierlo, and P. Van Den Bossche, "Critical review of state of health estimation methods of Li-ion batteries for real applications," *Renewable and Sustainable Energy Reviews*, vol. 56. Pergamon, pp. 572–587, Apr. 01, 2016. doi: 10.1016/j.rser.2015.11.042.

[7] A. G. Hsieh, S. Bhadra, B. J. Hertzberg, P. J. Gjeltema, A. Goy, J. W. Fleischer, and D. A. Steingart, "Electrochemical-acoustic time of flight: in operando correlation of physical dynamics with battery charge and health," *Energy Environ. Sci.*, vol. 8, no. 5, pp. 1569–1577, 2015, doi: 10.1039/C5EE00111K.

[8] L. Gold, T. Bach, W. Virsik, A. Schmitt, J. Muller, T. E. M. Staab, and G. Sextl, "Probing lithium-ion batteries' state-of-charge using ultrasonic transmission – Concept and laboratory testing," *J. Power Sources*, vol. 343, pp. 536–544, 2017, doi: 10.1016/j.jpowsour.2017.01.090.

[9] J. B. Robinson, M. Pham, M. D. R. Kok, T. M. M. Heenan, D. J. L. Brett, and P. R. Shearing, "Examining the Cycling Behaviour of Li-Ion Batteries Using Ultrasonic Time-of-Flight Measurements," *J. Power Sources*, vol. 444, no. September, p. 227318, 2019, doi: 10.1016/j.jpowsour.2019.227318.

[10] H. Popp, M. Koller, S. Keller, G. Glanz, R. Klambauer, and A. Bergmann, "State Estimation Approach of Lithium-Ion Batteries by Simplified Ultrasonic Time-of-Flight Measurement," *IEEE Access*, vol. 7, pp. 170992–171000, 2019, doi: 10.1109/ACCESS.2019.2955556.

[11] Z. Wang, G. Feng, D. Zhen, F. Gu, and A. Ball, "A review on online state of charge and state of health estimation for lithium-ion batteries in electric vehicles," *Energy Reports*, vol. 7, pp. 5141–5161, 2021, doi: 10.1016/j.egyr.2021.08.113.

[12] J. B. Robinson, M. Maier, G. Alster, T. Compton, D. J. L. Brett, and P. R. Shearing, "Spatially resolved ultrasound diagnostics of Li-ion battery electrodes," *Phys. Chem. Chem. Phys.*, vol. 21, no. 12, pp. 6354–6361, 2019, doi: 10.1039/c8cp07098a.

[13] H. Li and Z. Zhou, "Numerical simulation and experimental study of fluid-solid coupling-based air-coupled ultrasonic detection of stomata defect of lithium-ion battery," *Sensors (Switzerland)*, vol. 19, no. 10, 2019, doi: 10.3390/s19102391.

[14] J. B. Robinson, R. E. Owen, M. D. R. Kok, M. Maier, J. Majasan, M. Braglia, R. Stocker, T. Amietszajew, A. J. Roberts, R. Bhagat, D. Billsson, J. Z. Olson, J. Park, G. Hinds, A. Ahlberg Tidblad, D. J. L. Brett, and P. R. Shearing, "Identifying Defects in Li-Ion Cells Using Ultrasound Acoustic Measurements," *J. Electrochem. Soc.*, vol. 167, no. 12, p. 120530, 2020, doi: 10.1149/1945-7111/abb174.

[15] L. P. Bauermann, L. V. Mesquita, C. Bischoff, M. Drews, O. Fitz, A. Heuer, and D. Biro, "Scanning acoustic microscopy as a non-destructive imaging tool to localize defects inside battery cells," *J. Power Sources Adv.*, vol. 6, no. May, p. 100035, 2020, doi: 10.1016/j.powera.2020.100035.

[16] H. Zappen, G. Fuchs, A. Gitis, and D. U. Sauer, "In-operando impedance spectroscopy and ultrasonic measurements during high-temperature abuse experiments on lithium-ion batteries," *Batteries*, vol. 6, no. 2, 2020, doi: 10.3390/batteries6020025.

[17] R. J. Copley, D. Cumming, Y. Wu, and R. S. Dwyer-Joyce, "Measurements and modelling of the response of an ultrasonic pulse to a lithium-ion battery as a precursor for state of charge estimation," *J. Energy Storage*, vol. 36, no. February, 2021, doi: 10.1016/j.est.2021.102406.

[18] C. G. Manriquez-Padilla, I. Cueva-Perez, A. Dominguez-Gonzalez, D. A. Elvira-Ortiz, A. Perez-Cruz, and J. J. Saucedo-Dorantes, "State of Charge Estimation Model Based on Genetic Algorithms and Multivariate Linear Regression with Applications in Electric Vehicles," *Sensors*, vol. 23, no. 6, p. 2924, Mar. 2023, doi: 10.3390/s23062924.

[19] S. P. Kodali, K. Deb, S. Bandaru, P. Munshi, and N. N. Kishore, "Simulation Studies on a Genetic Algorithm Based Tomographic Reconstruction Using Time-of-Flight Data from Ultrasound Transmission Tomography."

[20] V. S. Medeiros, A. C. Kubrusly, and M. R. Jimenez, "2018 IEEE Congress on Evolutionary Computation, CEC 2018 - Proceedings," *2018 IEEE Congress on Evolutionary Computation, CEC 2018 - Proceedings*. IEEE, 2018.

[21] Y. Wu, Y. Wang, W. K. C. Yung, and M. Pecht, "Ultrasonic Health Monitoring of Lithium-Ion Batteries," *Electronics*, vol. 8, no. 7, p. 751, 2019, doi: 10.3390/electronics8070751.

[22] G. Davies, K. W. Knehr, B. Van Tassell, T. Hodson, S. Biswas, A. G. Hsieh, and D. A. Steingart, "State of Charge and State of Health Estimation Using Electrochemical Acoustic Time of Flight Analysis," *J. Electrochem. Soc.*, vol. 164, no. 12, pp. A2746–A2755, 2017, doi: 10.1149/2.1411712jes.

[23] Z. Deng, Z. Huang, Y. Shen, Y. Huang, H. Ding, A. Luscombe, M. Johnson, J. E. Harlow, R. Gauthier, and J. R. Dahn, "Ultrasonic Scanning to Observe Wetting and 'Unwetting' in Li-Ion Pouch Cells," *Joule*, vol. 4, no. 9, pp. 2017–2029, 2020, doi: 10.1016/j.joule.2020.07.014.

[24] W. Chang, C. Bommier, T. Fair, J. Yeung, S. Patil, and D. Steingart, "Understanding Adverse Effects of Temperature Shifts on Li-Ion Batteries: An Operando Acoustic Study," *J. Electrochem. Soc.*, vol. 167, no. 9, p. 090503, 2020, doi: 10.1149/1945-7111/ab6c56.

[25] K. W. Knehr, T. Hodson, C. Bommier, G. Davies, A. Kim, and D. A. Steingart, "Understanding Full-Cell Evolution and Non-chemical Electrode Crosstalk of Li-Ion Batteries," *Joule*, vol. 2, no. 6, pp. 1146–1159, 2018, doi: 10.1016/j.joule.2018.03.016.

[26] T. Hodson, S. Patil, and D. Steingart, "A Initial Exploration of Coupled Transient Mechanical and Electrochemical Behaviors in Lithium Ion Batteries," *J. Electrochem. Soc.*, 2021, doi: 10.1149/1945-7111/ac0f86.

[27] F. Ardila, "Catalan Numbers," *Math. Intell.*, vol. 38, no. 2, pp. 4–5, 2016, doi: 10.1007/s00283-016-9625-6.

[28] R. Stanley and E. W. Weisstein, “Catalan Number,” *MathWorld--A Wolfram Web Resource*, 2021. https://mathworld.wolfram.com/CatalanNumber.html (accessed Oct. 28, 2021).
[29] H. A. Amr, “A Review of Population-based Meta- Heuristic Algorithm A Review of Population-based Meta-Heuristic Algorithm,” *A Rev. Popul. Meta-Heuristic*, 2013.
[30] J. Dreo, “Dreaming of Metaheuristics,” 2007. http://nojhan.free.fr/metah/ (accessed Aug. 16, 2021).
[31] S. Katoch, S. S. Chauhan, and V. Kumar, *A review on genetic algorithm: past, present, and future*, vol. 80. Multimedia Tools and Applications, 2021. doi: 10.1007/s11042-020-10139-6.
[32] O. Bschorr and H. J. Raida, “One-Way Wave Equation Derived from Impedance Theorem,” *Acoustics*, vol. 2, no. 1, pp. 164–170, 2020, doi: 10.3390/acoustics2010012.
[33] P. Blanloeuil, L. R. Francis Rose, M. Veidt, and C. H. Wang, “Time reversal invariance for a one-dimensional model of contact acoustic nonlinearity,” *J. Sound Vib.*, vol. 394, pp. 515–526, 2017, doi: 10.1016/j.jsv.2017.01.050.
[34] Y. Fan, F. Gu, and A. Ball, “Modelling acoustic emissions generated by sliding friction,” *Wear*, vol. 268, no. 5–6, pp. 811–815, 2010, doi: 10.1016/j.wear.2009.12.010.
[35] Y. Permanasari, E. H. Harahap, and E. P. Ali, “Speech recognition using Dynamic Time Warping (DTW),” *J. Phys. Conf. Ser.*, vol. 1366, no. 1, 2019, doi: 10.1088/1742-6596/1366/1/012091.
[36] E. Keogh and C. A. Ratanamahatana, “Exact indexing of dynamic time warping,” *Knowl. Inf. Syst.*, vol. 7, no. 3, pp. 358–386, 2005, doi: 10.1007/s10115-004-0154-9.
[37] J. Gelb, “Imaging the 4D Microstructure Evolution of a Commercial 18650 Li-ion Battery,” 2017. [Online]. Available: https://www.zeiss.com/content/dam/Microscopy/us/download/pdf/application-notes/x-ray-microscopy/en_44_013_044_wp_imaging-the-4d_microstructures.pdf